

RESEARCH ARTICLE | NOVEMBER 01 2023


High-fidelity state-to-state modeling of hypersonic flow over a double cone

Xiaoyong Wang (王小永) ; Jinghui Guo (郭京辉)  ; Qizhen Hong (洪启臻) ; Sijia Li (李思佳) 



Physics of Fluids 35, 116101 (2023)

<https://doi.org/10.1063/5.0174079>



APL Machine Learning

2023 Papers with Best Practices in Data Sharing and Comprehensive Background

[Read Now](#)



High-fidelity state-to-state modeling of hypersonic flow over a double cone

Cite as: Phys. Fluids **35**, 116101 (2023); doi: [10.1063/5.0174079](https://doi.org/10.1063/5.0174079)

Submitted: 27 August 2023 · Accepted: 10 October 2023 ·

Published Online: 1 November 2023



View Online



Export Citation



CrossMark

Xiaoyong Wang (王小永),¹  Jinghui Guo (郭京辉),^{2,a)}  Qizhen Hong (洪启臻),¹  and Sijia Li (李思佳)² 

AFFILIATIONS

¹ State Key Laboratory of High Temperature Gas Dynamics, Institute of Mechanics, Chinese Academy of Sciences, 100190 Beijing, China

² School of Aeronautic Science and Engineering, Beihang University, Beijing 100191, China

^{a)} Author to whom correspondence should be addressed: guojinghui@buaa.edu.cn

ABSTRACT

The state-of-the-art high-fidelity state-to-state (StS) model is performed to investigate the hypersonic shock wave/laminar boundary layer interaction over a 25°–55° double cone. This work aims to clarify whether the shortcomings of thermochemical models are the underlying source for the discrepancies between the simulations and experiments. A high-enthalpy nitrogen flow with a Mach number of 11.54 and a unit Reynolds number of $4.394 \times 10^5/\text{m}$ is considered. We first find that the StS and widely used two-temperature models yield two different shock reflection patterns (i.e., the regular reflection and Mach reflection, respectively). However, the surface pressure and heat flux distributions predicted by the two models are generally consistent, which are not influenced by the differences in the shock patterns, dissociation rates, and non-Boltzmann vibrational distributions in the flowfields. Moreover, the StS model fails to match the experiments in spite of fairly limited improvement. Our findings indicate that the shortcomings of thermochemical models are not the main reason for the discrepancies in the simulations and experiments for the high-enthalpy nitrogen double-cone flow.

Published under an exclusive license by AIP Publishing. <https://doi.org/10.1063/5.0174079>

I. INTRODUCTION

Shock wave/boundary layer interaction (SWBLI) is a representative flow phenomenon for the hypersonic vehicle cruising at hypersonic speeds.¹ Understanding and accurately predicting the SWBLI is crucial for the design and control of the hypersonic vehicle because the SWBLI induces separation, peak heating, and unsteadiness.^{2,3} Hypersonic laminar flow over a double cone is a typical example of SWBLI. Extensive experiments and numerical approaches have been utilized to investigate the SWBLIs around double cones, in order to illustrate the complicated flow features and validate the numerical modeling capability.

A series of 25°–55° double-cone experiments, which were conducted in the LENS shock tunnels and expansion tunnel of Calspan-University at Buffalo Research Center (CUBRC), have provided essential measurement data sweeping a range of low ($<5 \text{ MJ/kg}$) to medium (about $5\text{--}6 \text{ MJ/kg}$) to high ($>7 \text{ MJ/kg}$) total enthalpies in nitrogen, oxygen, and air.⁴ Numerous investigations have been performed to examine the discrepancies between numerical simulations and experimental measurements.^{5,6} The length of shock-induced separation region and the distributions of surface pressure and heat flux were compared in detail. At high enthalpies, the length of the

separation region was severely underpredicted by simulations, and the pressure and heat flux distributions were not reasonably matched with experiments, although good agreement was achieved at low and medium enthalpies. Continuous works in the past two decades have found that these discrepancies can be attributed to deficient thermochemistry models,^{7–11} mis-specified freestream conditions,^{12,13} unsteadiness,^{12,14} three-dimensionality,¹⁵ and additional uncertainties.¹⁶ However, significant differences still remain, and the reasons for the discrepancies require to be clearly understood, especially for the cases at high enthalpies.

Among the aforementioned potential sources for the discrepancies, the shortcomings of thermochemical models are one of the issues that has received much attention. Research activities have continuously been motivated for the laminar hypersonic flows over double cones at high enthalpies, where thermochemical nonequilibrium effects play an important role. Park's two-temperature model has generally been implemented in the CFD simulations, which identified that the onset of separation occurs significantly later and the agreement of pressure and heat flux distributions is poor compared to experimental data.^{5,6,8,9,11} Even the inclusion of computed freestream conditions obtained by simulating the nonequilibrium flow through nozzle made

very limited improvement in the predictive capability.^{12,15} In addition, the catalytic wall assumption had weak effect on the predictions of the separation region extent.^{13,16} As the development in thermochemistry modeling, improved two-temperature models, which account for the vibration-chemistry coupling and the approximations of non-Boltzmann distributions, were used for the studies on high-enthalpy flows over double cones.^{7,10,11} However, these improved models yielded very similar results to the Park's model and still failed to reproduce the experimental measurements. In summary, the applicability of the widely used two-temperature model is limited. First, the non-Boltzmann effect is observed in the high-enthalpy thermochemical nonequilibrium flow simulation, contrary to the Boltzmann assumption used in the two-temperature model. Furthermore, the coefficients of chemical kinetic rates used in the two-temperature model were obtained by rearranging and fitting the decades-old shock-tube data, which contained a significant amount of uncertainties.

The high-fidelity state-to-state (StS) model has been proposed to overcome the deficiencies of the two-temperature model.¹⁷ In the StS model, each internal energy state is treated as a pseudo-species and its population is directly tracked, which can consequently resolve the non-Boltzmann distribution of internal energy. In addition, the rate coefficients for the excitation and dissociation processes of each internal energy state can be obtained by high-fidelity quasi-classical trajectory (QCT) computations.^{18–20} StS modeling has recently been implemented for the vibrational excitation and dissociation of oxygen, nitrogen, and air in the simulations of zero-dimensional isothermal/adiabatic reservoirs and one-dimensional postshock flows.^{18–23} Colonna *et al.*¹⁷ first performed realistic two-dimensional StS modeling of hypersonic air flows over a sphere. They concluded that the StS model provides better agreement with experimental results than the widely used two-temperature model, due to the strong effect of non-Boltzmann vibrational distribution on reaction rates. Furthermore, Ninni *et al.*^{24,25} performed two-dimensional simulations of high-enthalpy air flows over a double wedge, in which the thermochemical non-equilibrium effects were investigated by the StS and two-temperature models. They found that the transient location of the separation point predicted by the StS model is significantly earlier than the two-temperature model. However, their results were not compared with the experiment for further justification. Through the detailed analysis of high-enthalpy oxygen flow around a double cone, Ninni *et al.*¹³ also claimed that the StS modeling of nozzle expansion flow can yield a more accurate freestream condition, which would provide a better agreement in the flow structure with the experiment.

In this study, we seek the answers to the following questions: Can the high-fidelity thermochemical modeling results of SWBLI agree well with the experiments? Are the shortcomings of thermochemical models the underlying source for the discrepancies between the simulations and experiments? Consequently, the state-of-the-art high-fidelity StS model is first performed to simulate the two-dimensional axisymmetric hypersonic nitrogen flow over a double cone at high enthalpies. The sophisticated structure and non-equilibrium behavior in the double-cone flowfield are clearly presented. The separation length and surface properties are compared with experiments conducted at the CUBRC LENS-I facility.⁵ Furthermore, two more cases at higher enthalpies are investigated to testify the effect of thermochemical models with increasing extent of nonequilibrium. Finally, the conclusion is summarized.

II. THERMOCHEMICAL NONEQUILIBRIUM MODELS

The StS and two-temperature models are two typical methods to simulate high-enthalpy nitrogen flows. The governing equations and source terms for the two models are presented first, and the numerical methods are then illustrated.

A. State-to-state model

The governing equations for the StS model are expressed as¹⁷

$$\begin{cases} \frac{\partial \rho_{s,l}}{\partial t} + \frac{\partial \rho_{s,l} u_j}{\partial x_j} = \frac{\partial}{\partial x_j} \left(\rho D_s \frac{\partial y_{s,l}}{\partial x_j} \right) + \omega_{s,l} \\ \frac{\partial \rho u_i}{\partial t} + \frac{\partial \rho u_i u_j}{\partial x_j} = - \frac{\partial p}{\partial x_j} + \frac{\partial \tau_{ij}}{\partial x_j} \\ \frac{\partial \rho E}{\partial t} + \frac{\partial \rho H u_j}{\partial x_j} = \frac{\partial}{\partial x_j} \left(\eta \frac{\partial T}{\partial x_j} \right) + \frac{\partial}{\partial x_j} \left(\rho \sum_{s=1}^{ns} D_s \sum_{l=1}^{V_s} h_{s,l} \frac{\partial y_{s,l}}{\partial x_j} \right) + \frac{\partial \tau_{ij} u_i}{\partial x_j}, \end{cases} \quad (1)$$

where $\rho_{s,l}$, $y_{s,l}$, $h_{s,l}$, and $\omega_{s,l}$ denote the density, mass fraction, enthalpy, and source term of the s th species at the l th internal state, respectively. ns is the number of species, and V_s is the number of internal states for the s th species. ρ is the density, u_j is the j th velocity component, and E and H are the total energy and the total enthalpy per unit mass of mixture. D_s is the diffusion coefficient of the s th species, and η is the thermal conductivity for translational-rotational energy. τ_{ij} is the viscous stress tensor, T is the translational-rotational temperature, and p is the pressure calculated by Dalton law.

In this study, we focus on the excitation and dissociation of N_2 . In addition, N_2 includes 55 vibrational energy states. The mass production rate of N_2 at the l th vibrational state is calculated according to the vibrational-translational (VT) energy exchanges and dissociation-recombination (DR) chemical processes induced by N_2 - N_2 and N_2 -N collisions,²⁰ expressed as

$$\begin{aligned} \frac{N_A}{M_{N_2}} \omega_{N_2,l} = & \sum_{f \neq l} \left\{ k_{V-T}^N(f \rightarrow l) [N_2(f)] [N] - k_{V-T}^N(l \rightarrow f) [N_2(l)] [N] \right\} \\ & + \sum_{f \neq l} \left\{ k_{V-T}^{N_2}(f \rightarrow l) [N_2(f)] [N_2] \right. \\ & \left. - k_{V-T}^{N_2}(l \rightarrow f) [N_2(l)] [N_2] \right\} + k_{rec}^{N_2}(l) [N_2] [N]^2 \\ & - k_{dis}^N(l) [N_2(l)] [N_2] + k_{rec}^N(l) [N]^3 - k_{dis}^N(l) [N_2(l)] [N], \end{aligned} \quad (2)$$

where N_A is the Avogadro constant, M_{N_2} is the species molecular mass of N_2 , $k_{V-T}^{N_2}$ and k_{V-T}^N are the VT rates for the N_2 - N_2 and N_2 -N collisions.²⁰ $k_{dis}^{N_2}$ and $k_{rec}^{N_2}$ are the vibration-dissociation (VD) and recombination rates for N_2 - N_2 collision, and k_{dis}^N and k_{rec}^N are the VD and recombination rates for N_2 -N collision.²⁰ The square bracket $[\cdot]$ denotes the number density of species. Note that the vibration-vibration (VVT) energy transfer is neglected in the StS model.²⁰

The mass production rate of N is expressed as²⁰

$$\begin{aligned} \frac{N_A}{M_N} \omega_N = & 2 \sum_i \left\{ k_{dis}^{N_2} [N_2(i)] [N_2] - k_{rec}^{N_2} [N_2] [N]^2 + k_{dis}^N [N_2(i)] [N] \right. \\ & \left. - k_{rec}^N [N]^3 \right\}, \end{aligned} \quad (3)$$

where M_N is the species molecular mass of N.

Based on the N_4 potential energy surface and quasi-classical-trajectory method, high-fidelity VT and VD rates for N_2 - N_2 and N_2 - N collisions proposed by Fangman and Andrienko²⁰ are used. The temperature ranges for the VD and VT rates are 5000 – 30 000 K.

The VD rates for the N_2 - N_2 and N_2 - N collisions are fitted to a modified Arrhenius expression,

$$k_{\text{dis}}^{\text{sys}}(l) = \exp(A_l^{\text{sys}}) T^{B_l^{\text{sys}}} \exp\left(-\frac{C_l^{\text{sys}}}{T}\right), \quad (4)$$

where the superscript sys represents either the N_2 - N_2 or the N_2 - N system. T is the translational temperature, and A_l , B_l , and C_l are the constants for dissociation.²⁰

The VT rates for the N_2 - N_2 and N_2 - N collisions are fitted as

$$k_{V-T}^{\text{sys}}(f \rightarrow l) = 10^{-14} \exp\left(\alpha_{f \rightarrow l}^{\text{sys}} + \frac{\beta_{f \rightarrow l}^{\text{sys}}}{\ln(T)} + \gamma_{f \rightarrow l}^{\text{sys}} \ln(T) + \delta_{f \rightarrow l}^{\text{sys}} (\ln(T))^2\right), \quad (5)$$

where α , β , γ , and δ are the constants for VT transitions.²⁰

B. Two-temperature model

Under the two-temperature assumptions, the governing equations for chemically reacting viscous flows are expressed as²⁶

$$\left\{ \begin{aligned} \frac{\partial \rho_s}{\partial t} + \frac{\partial \rho_s u_j}{\partial x_j} &= \frac{\partial}{\partial x_j} \left(\rho D_s \frac{\partial y_s}{\partial x_j} \right) + \omega_s \\ \frac{\partial \rho u_i}{\partial t} + \frac{\partial \rho u_i u_j}{\partial x_j} &= -\frac{\partial p}{\partial x_j} + \frac{\partial \tau_{ij}}{\partial x_j} \\ \frac{\partial \rho E_v}{\partial t} + \frac{\partial \rho E_v u_j}{\partial x_j} &= \frac{\partial}{\partial x_j} \left(\eta_v \frac{\partial T_v}{\partial x_j} \right) \\ &+ \frac{\partial}{\partial x_j} \left(\rho \sum_{s=1}^{ns} h_{v,s} D_s \frac{\partial y_s}{\partial x_j} \right) + \omega_v \\ \frac{\partial \rho E}{\partial t} + \frac{\partial \rho H u_j}{\partial x_j} &= \frac{\partial}{\partial x_j} \left(\eta_v \frac{\partial T_v}{\partial x_j} + \eta \frac{\partial T}{\partial x_j} \right) \\ &+ \frac{\partial}{\partial x_j} \left(\rho \sum_{s=1}^{ns} h_s D_s \frac{\partial y_s}{\partial x_j} \right) + \frac{\partial \tau_{ij} u_i}{\partial x_j}, \end{aligned} \right. \quad (6)$$

where ρ_s and y_s are the density and mass fraction of species s , and E_v , T_v , and η_v are the vibrational energy, temperature, and thermal conductivity. $h_{v,s}$ and h_s are the vibrational and total enthalpy per unit mass of species s .

The two-temperature model assumes each internal energy to follow a Boltzmann distribution corresponding to its equilibrium temperature. The mass production rate of species s due to the chemical reactions is expressed as²⁷

$$\omega_s = M_s \sum_{r=1}^{nr} (\beta_{rs} - \alpha_{rs}) \left[k_{f,r} \prod_{s=1}^{ns} \left(\frac{\rho_s}{M_s} \right)^{\alpha_{rs}} - k_{b,r} \prod_{s=1}^{ns} \left(\frac{\rho_s}{M_s} \right)^{\beta_{rs}} \right], \quad (7)$$

where nr and ns are the number of reactions and species, α_{rs} and β_{rs} are the stoichiometric coefficients for reactants and products, and $k_{f,r}$ and $k_{b,r}$ are the forward and backward rates for the reaction r .

The forward reaction rates are expressed by the semi-empirical Arrhenius equation,²⁸

$$k_{f,r} = C_r T_c^{\eta_r} \exp\left(-\frac{\theta_r}{T_c}\right), \quad (8)$$

where T_c is the controlling temperature, and C_r , η_r , and θ_r are the reaction constants. The backward rates are evaluated based on the detailed balance theory.²⁸

In the two-temperature model, the vibration-dissociation coupling effect is considered in two ways. To demonstrate the effect of vibrational nonequilibrium on the dissociation rates, T_c is expressed as a function of T and T_v according to Park's analysis for shock-tube experiment,²⁹

$$T_c = T^\alpha T_v^{1-\alpha}, \quad (9)$$

where α is generally equal to 0.5 or 0.7. In this study, $T_c = \sqrt{TT_v}$ and T_v is the vibrational temperature.

On the other hand, the source term of vibrational energy ω_v is governed as²⁸

$$\omega_v = \rho \frac{E_v(T) - E_v(T_v)}{\tau_v} + \omega_{vd}, \quad (10)$$

where the first term is the translational-vibrational energy transfer rate based on the Landau-Teller model,²⁸ and τ_v is the vibrational relaxation time evaluated by Millikan-White's formula.²⁸ Due to the widely used non-preferential model, the vibrational energy change per dissociation ω_{vd} is expressed as²⁸

$$\omega_{vd} = \sum_{s=1}^{ns} \omega_s e_{v,s}, \quad (11)$$

which assumes that the loss of vibrational energy is the average vibrational energy $e_{v,s}$.

C. Numerical methods

The axisymmetric equations for the StS and two-temperature models are resolved by an in-house code named ARTIST-CFD.²⁶ Inviscid fluxes are computed by the modified Steger-Warming upwind scheme with second-order MUSCL reconstruction and minmod limiter,^{26,28} and a second-order central difference scheme is applied for discretization of viscous fluxes. The data-parallel line relaxation (DPLR) scheme is used for time advancement.²⁸ Species viscosities and thermal conductivities are calculated by Blottner's curve fits and Eucken's relation, respectively.^{28,30} The mixture transport coefficients are obtained by Wilke's semiempirical mixing rule.^{28,30} The species mass diffusion coefficient is calculated assuming a constant Lewis number, and its value is equal to 1.4.^{28,30} Species mass diffusion fluxes are calculated by a modified Fick's model to guarantee that the sum of diffusion fluxes is zero.^{28,31}

III. COMPUTATIONAL DETAILS

Run 46 (denoted as case 1) in the series of the 25°–55° double-cone experiments conducted at the CUBRC LENS-I facility⁵ is considered. The freestream conditions are listed in Table I. To investigate the influence of nonequilibrium extent, two more cases (i.e., cases 2 and 3) are created by increasing the total enthalpy H_0 through only improving u_∞ .

TABLE I. Freestream conditions.

Case	H_0 (MJ/kg)	Ma_∞	Re_∞ ($10^3/m$)	u_∞ (m/s)	ρ_∞ (g/m^3)	T_∞ (K)	$T_{v,\infty}$ (K)	$c_{N_2,\infty}$	$c_{N,\infty}$
1	8.6	11.54	439.4	3946.9					
2	12.9	14.38	547.9	4919.4	1.958	281.7	3072	0.998 42	0.001 58
3	17.2	16.72	637.4	5723.0					

The computational grid consisting of 1024×512 nodes is axisymmetrically constructed in the axial and radial directions, respectively. The normal spacing of the first layer near surface is specified to be 1×10^{-7} m to guarantee that the cell Reynolds number is approximately on the order of magnitude of unity.⁷ This grid resolution has been validated to be independent for the simulation of hypersonic high-enthalpy double-cone flows.^{7,10} The wall boundary condition is assumed noncatalytic with a constant temperature of 296.3 K.^{5,8}

IV. RESULTS

A. Base flows

As illustrated in Figs. 1(a) and 1(b), the SWBLI structure predicted by the StS model is generally similar to that by the two-temperature model. An attached oblique shock of the first cone interacts with a strong detached bow shock of the second cone. This interaction produces a transmitted shock, forming a triple point. The transmitted shock interacts with a reattachment shock and impinges on the second cone, which results in the intense pressure increase and severe heat transfer. The strong adverse pressure gradient causes the upstream separation region that creates a separation shock, which in turn affects the transmitted shock and adverse pressure gradient.³²

The comparison of Mach number distributions for the StS and two-temperature models is shown in Fig. 2. Slight difference obtained by these two models is demonstrated in the regions behind the detached shock, where significant thermal and chemical nonequilibrium occurs.^{8,9} The StS model predicts the larger stand-off distance behind the detached shock than the two-temperature model. Accordingly, the triple point and the transmitted shock move closer to the juncture of two cones.

The shock interactions predicted by the StS and two-temperature models can be identified as type V interaction.^{33,34} However, two different shock reflection patterns can still be observed in the interaction of the transmitted and reattachment shocks. The pattern predicted by the StS model is a regular reflection (RR), while that by the two-temperature model is a Mach reflection (MR).³⁴ Previous study of inviscid hypersonic double-wedge flows has shown that $RR \rightarrow MR$ transition occurs with a slight increase in the second wedge angle from 40.2° to 40.5° .³⁴ This study indicates that the slight difference of detached shock could also induce $RR \rightarrow MR$ transition.

To elucidate the difference in the detached shock between the two models, the profiles of flow properties along a typical streamline are compared in Fig. 3. As shown in Fig. 2, the streamline intersects the detached shock in the vicinity of triple point. Note that the

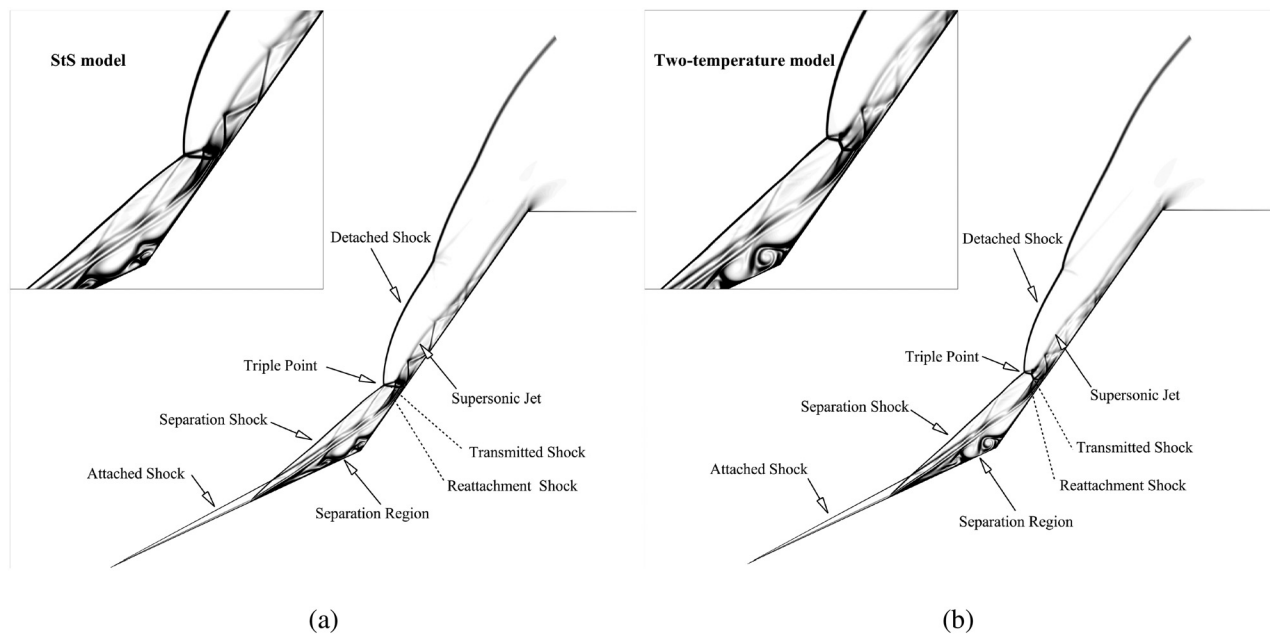


FIG. 1. Flowfield structures around the double cone ($H_0 = 8.4$ MJ/kg, contoured by the density gradient magnitude). (a) StS model and (b) two-temperature model.

08 April 2024 03:53:56

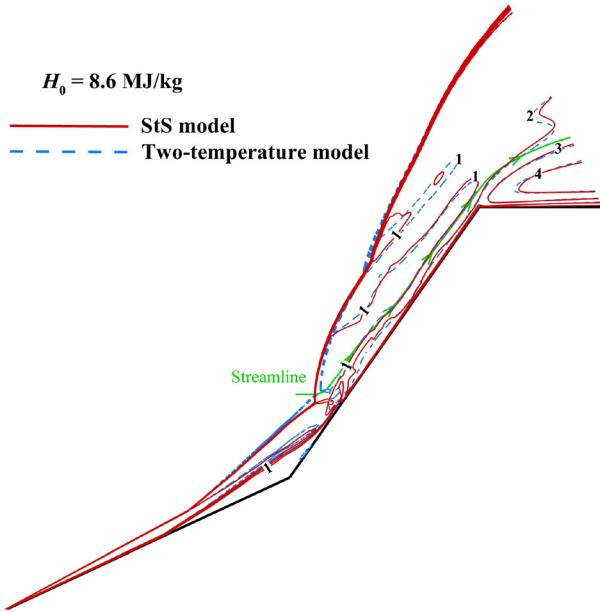


FIG. 2. Contours of Mach number predicted by the StS and two-temperature models ($H_0 = 8.4$ MJ/kg).

vibrational temperature T_v is calculated from the StS results, which is expressed by¹⁹

$$\frac{\sum_i n_i e_{v,i}}{\sum_i n_i} = \frac{\sum_i e_{v,i} \exp(-e_{v,i}/k_B T_v)}{\sum_i \exp(-e_{v,i}/k_B T_v)}, \quad (12)$$

where n_i and $e_{v,i}$ are the mole number and vibrational energy at the i th vibrational state, respectively. k_B is the Boltzmann constant.

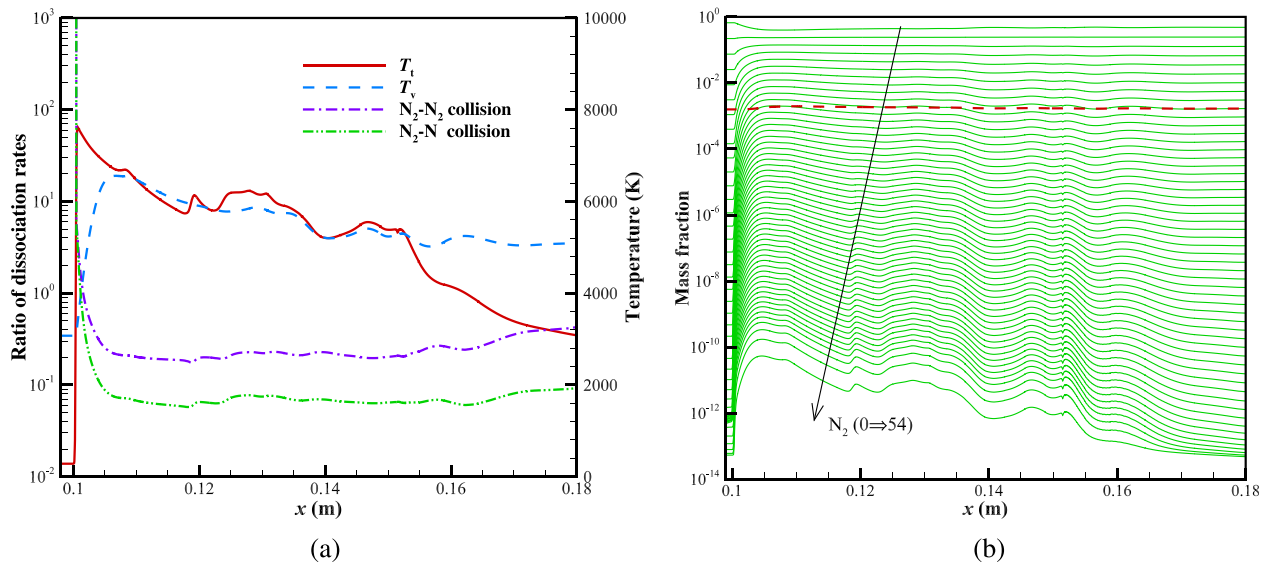


FIG. 3. Profiles along the streamline ($H_0 = 8.4$ MJ/kg). (a) Rates and temperature and (b) mass fraction. Green solid lines denote the mass fraction of the vibrational energy states of N_2 , and red dashed line denotes the mass fraction of N.

The total dissociation rate by the StS model is tallied up as the sum of the dissociation rate at each vibrational state,²⁶

$$k_{f,StS} = \sum_l k_{dis}^{sys}(l) \frac{[N_2(l)]}{[N_2]}, \quad (13)$$

where the superscript sys represents either the N_2 - N_2 or the N_2 -N system.

For comparison, the dissociation rate by the two-temperature model is calculated by Eq. (8). Note that T and T_v used to compute T_c for dissociation are yielded from the StS model rather than the two-temperature results, and thus, possible influence of other flowfield disparities on the dissociation rate is removed.

It is identified that the flow region along the streamline can be classified into three parts due to the featured thermochemical nonequilibrium states, as shown in Figs. 3(a) and 3(b). First, T pronouncedly rises behind the detached shock, and the vibrational energy is successively excited with a sharp increase in T_v due to VT energy transfer. Accordingly, the mass fractions of N_2 at high vibrational levels evidently increase. Meanwhile, N_2 keeps dissociating, maintaining the number density of N at a certain degree. Because the molecules at high vibrational levels are preferential to dissociate, their number densities drop more rapidly. Due to the competition between VT energy transfer and dissociation,^{17,19} T_v reaches its peak value. Downstream, dissociation begins to dominate the nonequilibrium process, leading to the gradual decreases in T_v and number densities of N_2 especially at high vibrational levels. In the vicinity of peak T_v location, the vibrational energy begins to approach equilibrium with translational energy. In general, T is virtually equal to T_v and also decreases. Eventually in the expansion region, the vibrational energy is virtually frozen and T_v almost keeps constant, while T greatly decreases since translational energy is substantially converted into kinetic energy. Note that the mass fraction of N virtually keeps constant along the whole streamline.

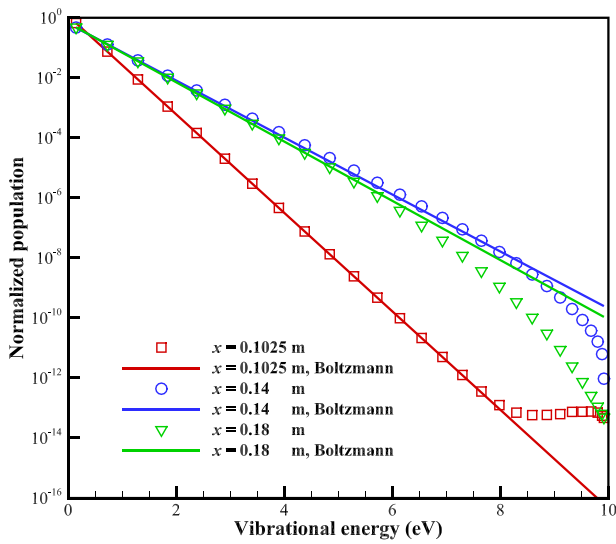


FIG. 4. Number density distributions of vibrational energy states for N_2 along the streamline ($H_0 = 8.4$ MJ/kg).

To better understand the nonequilibrium deviation of vibrational distributions behind the detached shock, the number densities of vibrational levels calculated by the StS model along the streamline are plotted in Fig. 4, by comparing the corresponding Boltzmann distributions conforming to the average vibrational temperature [see Eq. (12)]. Three representative probes ($x = 0.1025$ m, $x = 0.14$ m, and $x = 0.18$ m) are selected from the vibrational excitation, thermal equilibrium, and vibrational frozen regions, according to the typical divisions identified above. At $x = 0.1025$ m, the N_2 vibrational distribution deviates from the corresponding Boltzmann one with the high vibrational levels displaying an overpopulation due to vibrational excitation by VT energy

transfer. As the dissociation dominates in the thermal equilibrium region (at $x = 0.14$ m), the number densities at high vibrational levels decrease, leading to an underpopulation. In the expansion region (at $x = 0.18$ m), T_v is higher than T , and thus, the other thermal nonequilibrium appears with vibrational de-excitation by the energy transfer from vibrational to translational states. The number densities at high vibrational levels decline more, and lower lying levels depart from a Boltzmann distribution, leading to a stronger underpopulation than that at $x = 0.14$ m. It can be stated that the vibrational excitation and de-excitation by VT energy transfer as well as the dissociation induced vibrational energy loss preferentially display as the overpopulation or the underpopulation of number densities at high vibrational levels.

Furthermore, the ratios of dissociation rates by the StS relative to two-temperature model are less than one in the large extent behind the detached shock [see Fig. 3(a)], indicating that the two-temperature model overpredicts the dissociation rates. Specifically, the ratios dramatically decrease in the region of vibrational excitation, which suggests that the difference in the rates between these two models enlarges due to vibrational nonequilibrium. In contrast, in the thermal equilibrium region, the ratios keep nearly constant with the values less than 0.5 and 0.1 for the N_2-N_2 and N_2-N collisions, respectively. In the vibrational frozen region, the ratios slightly increase, which may be due to the drop in T . In general, the difference in the dissociation rates between the two models is larger for the N_2-N than N_2-N_2 collisions.

It is observed that the dissociation rates obtained by the two models are different and the vibrational levels of N_2 obey non-Boltzmann distributions. It has been proven that the reaction rates are greatly influenced by the non-Boltzmann vibrational distributions.¹⁷ However, the two-temperature model overestimates dissociation rates due to the assumption of Boltzmann vibrational distributions and the dependence of rate coefficients on the controlling temperature, which gives rise to a reduction in the translational temperature and thus an increase in the density behind the detached shock.³⁵ As a consequence, the StS model can predict a larger and theoretically more accurate

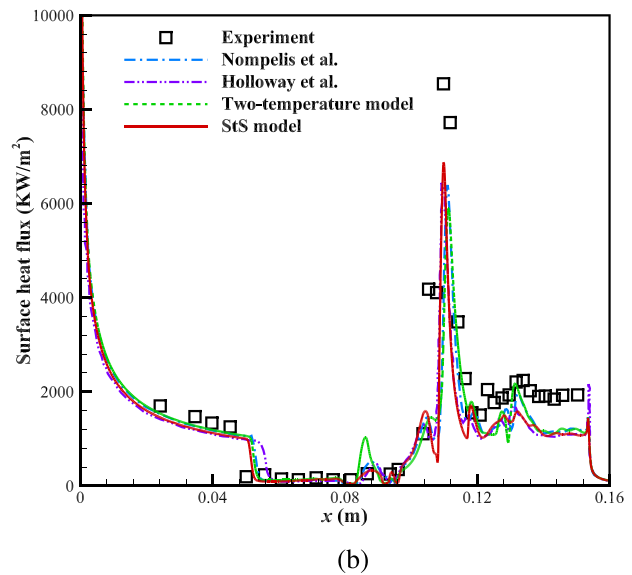
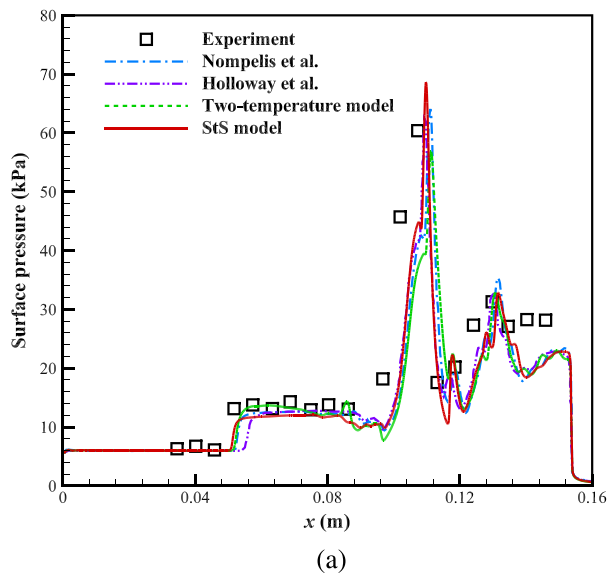


FIG. 5. Surface properties ($H_0 = 8.4$ MJ/kg). (a) Pressure and (b) heat flux.

TABLE II. The separation region obtained by the StS and two-temperature models.

Case	Descriptions (unit: cm)	StS model	Two-temperature model	Difference, %
1	Separation point	5.1695	5.2527	-1.58
	Reattachment point	10.959	11.070	-1.00
	Length of separation region	5.7894	5.8173	-0.48
2	Separation point	6.4661	6.6607	-2.92
	Reattachment point	10.367	10.351	0.16
	Length of separation region	3.9010	3.6903	5.71
3	Separation point	7.4416	7.4808	-0.52
	Reattachment point	10.027	10.077	-0.50
	Length of separation region	2.5857	2.5966	-0.42

stand-off distance of the detached shock than the two-temperature model.³⁶

B. Surface properties

The comparisons of surface pressure and heat flux obtained by the StS and two-temperature models with the experimental measurements⁵ and prior simulations^{5,9} are shown in Fig. 5. The lengths of separation region obtained by the two models are illustrated in Table II.

For case 1, the StS model predicts slightly earlier separation and reattachment locations than the two-temperature model, while the length of separation region does not change substantially with a relative difference of only -0.48%. Based on the CUBRC experimental measurements, the location of separation point was estimated as

$x = 4.8$ cm.⁹ Note that the separation location predicted by the StS model is closer to the experiments than the two-temperature model. However, all the models underestimate the length of separation region as compared to the experiment. In addition, the peak pressure and heat flux predicted by the StS model are higher than those by the two-temperature model by 21.12% and 16.83%, respectively. However, the peak pressure and heat flux predicted by the two models are in poor agreement with experiments. For the StS model, the relative errors of peak pressure and heat flux to the experiments are 15.31% and -19.42%, respectively. Downstream the peaks of pressure and heat flux, the pressure on the second cone is virtually the same for the two models, and there is a minor difference in the heat flux distributions, both of which are, in general, slightly lower than the experimental data.

Generally, the surface pressure and heat flux distributions predicted by the two models are consistent, although there are differences in the shock patterns, dissociation rates, and vibrational distributions in the flowfields between the two models. The StS model leads to an earlier location of separation point as well as higher peaks of pressure and heat flux than the two-temperature model. However, the StS model also fails to match the experiments in spite of slight improvement.

C. Effect of total enthalpy

For the higher total enthalpy cases, the double-cone flowfield structures predicted by the StS and two-temperature models are compared in Fig. 6, and the surface properties are compared in Fig. 7. The lengths of separation region obtained by the two models are also illustrated in Table II.

The StS and two-temperature models still produce very similar flowfield structures. Minimal differences mainly lie in the detached shock layer, especially the stand-off distances. A slightly larger stand-

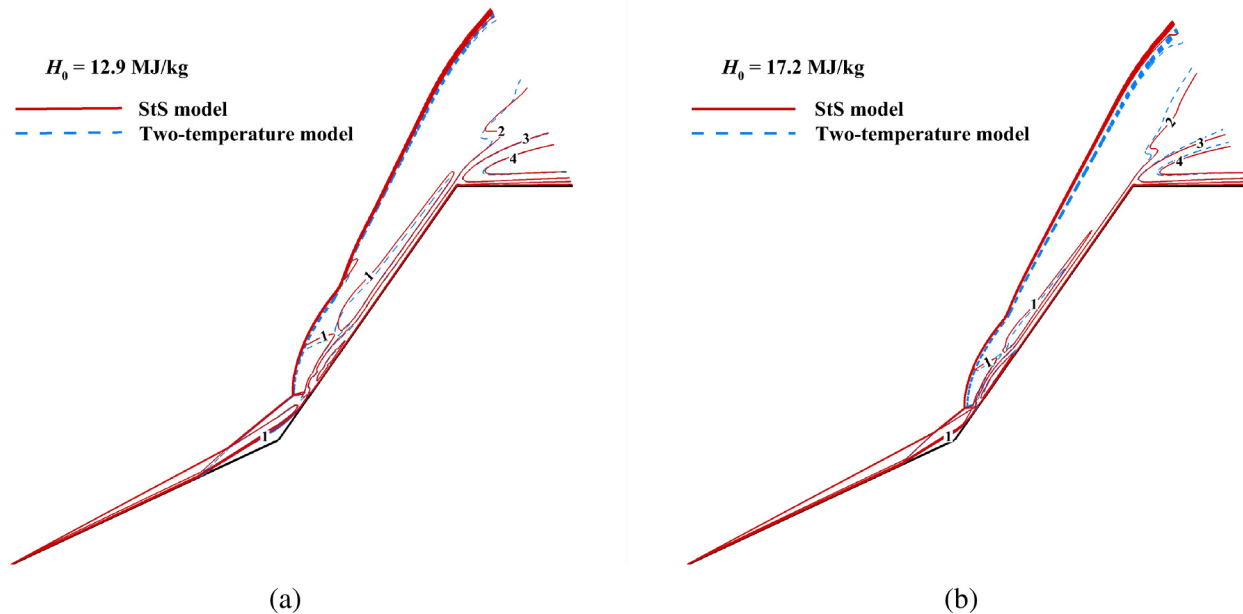


FIG. 6. Contours of Mach number predicted by the StS and two-temperature models. (a) Case: $H_0 = 12.9$ MJ/kg and (b) case: $H_0 = 17.2$ MJ/kg.

off distance of the detached shock is predicted by the StS model than by the two-temperature model. For the two cases, an earlier flow separation is predicted by the StS model than the two-temperature model. For the $H_0 = 12.9$ MJ/kg case, the length of separation region predicted by the StS model is larger than that of the two-temperature model by 5.71%, showing the biggest difference among all the cases. In contrast, the difference in the length of separation region between these two models is minimal as -0.42% for the $H_0 = 17.2$ MJ/kg case. As shown, the difference in the length of separation region predicted by the StS and two-temperature models does not monotonically increase with H_0 . The relative differences in the peak pressure and heat flux predicted by the StS model to the two-temperature model are 6.38% and -5.78% for the $H_0 = 12.9$ MJ/kg case, as well as 6.30% and

21.88% for the $H_0 = 17.2$ MJ/kg case. It is also shown that the difference in the peak heat flux between the two models varies substantially but does not monotonically increase with H_0 . In general, at higher enthalpies, the distributions of pressure and heat flux predicted by the StS model are nearly the same as those of two-temperature model. The StS model cannot significantly improve the predictive accuracy of hypersonic nonequilibrium double-cone flow.

V. CONCLUSION

Hypersonic high-enthalpy nitrogen flows over a 25° - 55° double cone are numerically investigated by the state-of-the-art high-fidelity StS and widely used two-temperature models. The main findings are as follows:

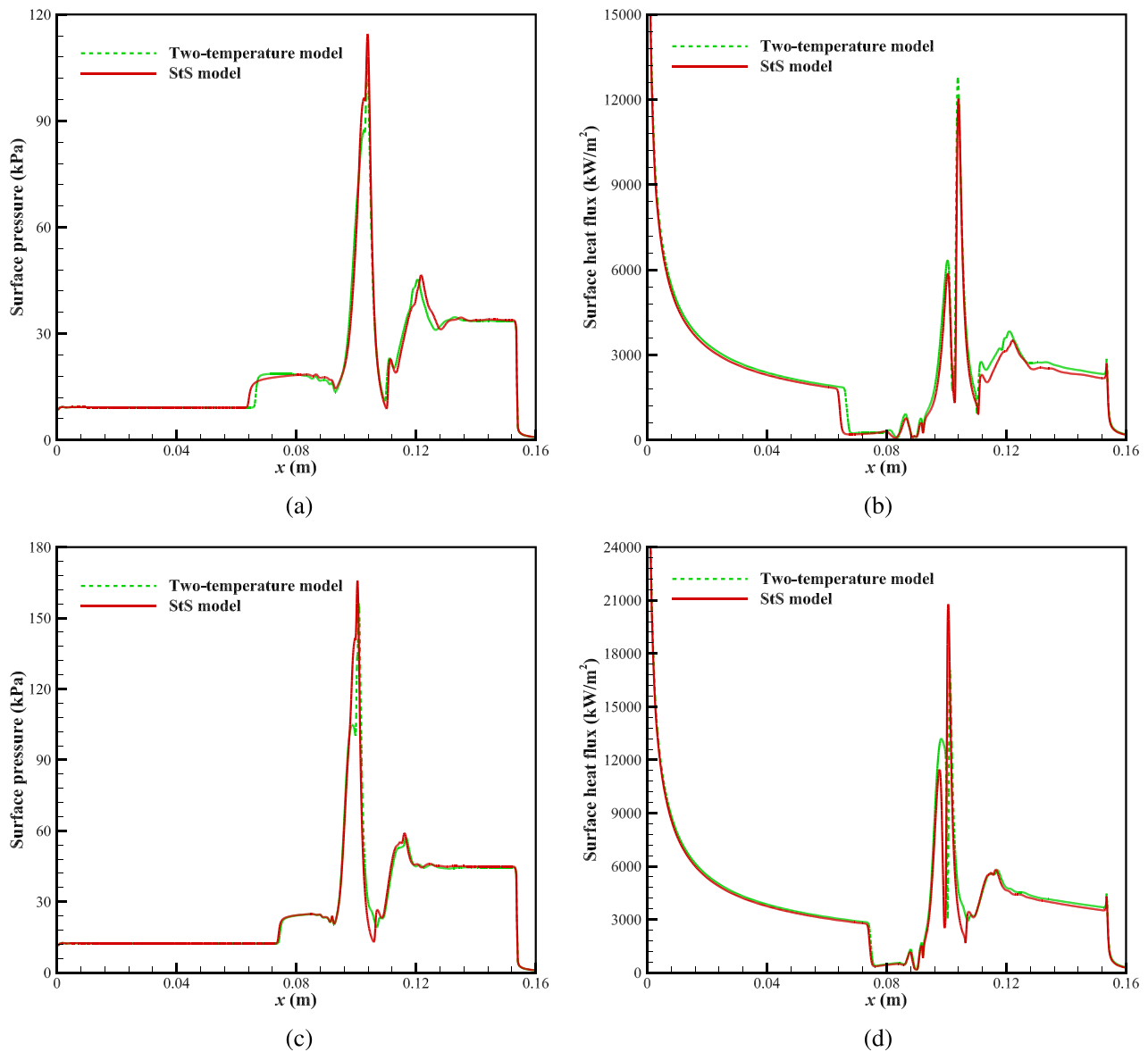


FIG. 7. Surface properties. (a) Pressure ($H_0 = 12.9$ MJ/kg); (b) heat flux ($H_0 = 12.9$ MJ/kg); (c) pressure ($H_0 = 17.2$ MJ/kg); and (d) heat flux ($H_0 = 17.2$ MJ/kg).

08 April 2024 03:53:56

- The flowfield structures obtained by the two models are similar. Small differences are shown as the slightly larger stand-off distance of the detached shock predicted by the StS model, which is attributed to an overprediction of dissociation rates by the two-temperature model. Moreover, two different shock reflection patterns, i.e., regular reflection and Mach reflection, are obtained by the StS and two-temperature models, respectively.
- These two models also produce nearly consistent distributions of surface pressure and heat flux. The differences in the shock patterns, dissociation rates, and vibrational distributions in the flowfields predicted by the two models do not induce significant disparities in the surface pressure and heat flux. Small differences are shown by the StS model leading to a slightly earlier location of separation point. Additionally, the disparities in the peaks of surface pressure and heat flux are observed between the two models.
- The StS model still fails to reproduce the experiments despite fairly limited enhancement in agreement with the experiments. Both models still underestimate the length of separation region, and the predicted heat flux and pressure are not well matched with the experiments for the $H_0 = 8.6$ MJ/kg case. Furthermore, the extension to higher total enthalpies indicates that the differences in the length of separation region and the peak heat flux between the two models do not monotonically increase with the total enthalpy.

Therefore, it can be concluded that the shortcomings of the thermochemical models are not the main reason for the discrepancies in the simulations and experiments for the high-enthalpy nitrogen double-cone flow. Future work will emphasize on the influence of flow unsteadiness and nonuniformity, which may be expected to elucidate the source for the discrepancies.

ACKNOWLEDGMENTS

This work was supported by the National Natural Science Foundation of China (Grant Nos. 12002348 and 12102025) and the Double First Class University Plan (Grant No. 030810-ZG216S2312).

AUTHOR DECLARATIONS

Conflict of Interest

The authors have no conflicts to disclose.

Author Contributions

Xiaoyong Wang: Conceptualization (equal); Methodology (equal); Software (equal); Writing – original draft (equal). **Jinghui Guo:** Conceptualization (equal); Methodology (equal); Writing – original draft (equal). **Qizhen Hong:** Conceptualization (equal); Writing – review & editing (equal). **Sijia Li:** Writing – review & editing (equal).

DATA AVAILABILITY

The data that support the findings of this study are available from the corresponding author upon reasonable request.

REFERENCES

- ¹J. D. J. Anderson, *Hypersonic and High-Temperature Gas Dynamics*, 3rd ed. (American Institute of Aeronautics and Astronautics, 2019).

- ²D. V. Gaitonde, “Progress in shock wave/boundary layer interactions,” *Prog. Aerosp. Sci.* **72**, 80–99 (2015).
- ³D. V. Gaitonde and M. C. Adler, “Dynamics of three-dimensional shock-wave/boundary-layer interactions,” *Annu. Rev. Fluid Mech.* **55**, 291–321 (2023).
- ⁴M. S. Holden, “Experimental research and analysis in supersonic and hypervelocity flows in the LENS shock tunnels and expansion tunnel,” AIAA Paper No. 2015-3660, 2015.
- ⁵I. Nompelis, G. V. Candler, M. S. Holden, and T. P. Wadhams, “Computational investigation of hypersonic viscous/inviscid interactions in high enthalpy flows,” AIAA Paper No. 2003-3642, 2003.
- ⁶I. Nompelis and G. Candler, “Numerical investigation of double-cone flow experiments with high-enthalpy effects,” AIAA Paper No. 2010-1283, 2010.
- ⁷J. Hao, J. Wang, and C. Lee, “Numerical simulation of high-enthalpy double-cone flows,” *AIAA J.* **55**, 2471–2475 (2017).
- ⁸N. Kianvashrad and D. D. Knight, “Nonequilibrium effects on prediction of aerothermodynamic loading for a double cone,” *AIAA J.* **57**, 2946–2963 (2019).
- ⁹M. E. Holloway, K. M. Hanquist, and I. D. Boyd, “Assessment of thermochemistry modeling for hypersonic flow over a double cone,” *J. Thermophys. Heat Transfer* **34**, 538–547 (2020).
- ¹⁰J. Gao, J. Hao, J. Wang, and C. Lee, “Effect of thermochemical nonequilibrium modeling on high-enthalpy double-cone flow,” *J. Spacecr. Rockets* **58**, 1243–1247 (2021).
- ¹¹M. E. Holloway, R. S. Chaudhry, and I. D. Boyd, “Assessment of hypersonic double-cone experiments for validation of thermochemistry models,” *J. Spacecr. Rockets* **59**, 389–400 (2022).
- ¹²I. Nompelis, G. Candler, M. MacLean, T. Wadhams, and M. Holden, “Numerical investigation of high enthalpy chemistry on hypersonic double-cone experiments,” AIAA Paper No. 2005-584, 2005.
- ¹³D. Ninni, F. Bonelli, G. Colonna, and G. Pascazio, “On the influence of non equilibrium in the free stream conditions of high enthalpy oxygen flows around a double-cone,” *Acta Astronaut.* **201**, 247–258 (2022).
- ¹⁴D. Knight, J. Longo, D. Drikakis, D. Gaitonde, A. Lani, I. Nompelis, B. Reimann, and L. Walpot, “Assessment of CFD capability for prediction of hypersonic shock interactions,” *Prog. Aeronaut. Sci.* **48–49**, 8–26 (2012).
- ¹⁵J. Ray, S. Kieweg, D. Dinzl, B. Carnes, V. G. Weirs, B. Freno, M. Howard, T. Smith, I. Nompelis, and G. V. Candler, “Estimation of inflow uncertainties in laminar hypersonic double-cone experiments,” *AIAA J.* **58**, 4461–4474 (2020).
- ¹⁶I. Nompelis and G. V. Candler, “US3D predictions of double-cone and hollow cylinder-flare flows at high-enthalpy (Invited),” AIAA Paper No. 2014-3366, 2014.
- ¹⁷G. Colonna, F. Bonelli, and G. Pascazio, “Impact of fundamental molecular kinetics on macroscopic properties of high-enthalpy flows: The case of hypersonic atmospheric entry,” *Phys. Rev. Fluids* **4**, 033404 (2019).
- ¹⁸J. G. Kim and I. D. Boyd, “State-resolved master equation analysis of thermochemical nonequilibrium of nitrogen,” *Chem. Phys.* **415**, 237–246 (2013).
- ¹⁹Q. Hong, X. Wang, Y. Hu, and Q. Sun, “Development of a stagnation streamline model for thermochemical nonequilibrium flow,” *Phys. Fluids* **32**, 046102 (2020).
- ²⁰A. J. Fangman and D. A. Andrienko, “Vibrational-specific model of simultaneous N_2-N and N_2-N_2 relaxation under postshock conditions,” *J. Thermophys. Heat Transfer* **36**, 568–583 (2022).
- ²¹M. Panesi, A. Munafò, T. E. Magin, and R. L. Jaffe, “Nonequilibrium shock-heated nitrogen flows using a rovibrational state-to-state method,” *Phys. Rev. E* **90**, 013009 (2014).
- ²²D. A. Andrienko and I. D. Boyd, “High fidelity modeling of thermal relaxation and dissociation of oxygen,” *Phys. Fluids* **27**, 116101 (2015).
- ²³K. Neitzel, D. Andrienko, and I. D. Boyd, “Aerothermochemical nonequilibrium modeling for oxygen flows,” *J. Thermophys. Heat Transfer* **31**, 634–645 (2017).
- ²⁴D. Ninni, F. Bonelli, G. Colonna, and G. Pascazio, “Unsteady behavior and thermochemical non equilibrium effects in hypersonic double-wedge flows,” *Acta Astronaut.* **191**, 178–192 (2022).
- ²⁵G. Pascazio, D. Ninni, F. Bonelli, and G. Colonna, “Hypersonic flows with detailed state-to-state kinetics using a GPU cluster,” in *Plasma Modeling Methods and Applications*, 2nd ed. (IOP Publishing, Bristol, UK, 2022), pp. 10–11.

- ²⁶X. Wang, Q. Hong, Y. Hu, and Q. Sun, "On the accuracy of two-temperature models for hypersonic nonequilibrium flow," *Acta Mech. Sin.* **39**, 122193 (2023).
- ²⁷X. Wang, C. Yan, Y. Zheng, and E. Li, "Assessment of chemical kinetic models on hypersonic flow heat transfer," *Int. J. Heat Mass Transfer* **111**, 356–366 (2017).
- ²⁸L. C. Scalabrin, "Numerical simulation of weakly ionized hypersonic flow over reentry capsules," Ph.D. thesis (University of Michigan, 2007).
- ²⁹C. Park, *Nonequilibrium Hypersonic Aerothermodynamics* (Wiley-Interscience, 1990).
- ³⁰H. Alkandry, I. D. Boyd, and A. Martin, "Comparison of transport properties models for flowfield simulations of ablative heat shields," *J. Thermophys. Heat Transfer* **28**, 569–582 (2014).
- ³¹Y. Tian, G. Lin, and J. Guo, "Analysis of mass diffusion theory and models for high-temperature multi-component gases," *Int. J. Heat Mass Transfer* **181**, 121994 (2021).
- ³²H. Babinsky and J. K. Harvey, *Shock Wave-Boundary-Layer Interactions* (Cambridge University Press, 2011).
- ³³J. Olejniczak, M. J. Wright, and G. V. Candler, "Numerical study of inviscid shock interactions on double-wedge geometries," *J. Fluid Mech.* **352**, 1–25 (1997).
- ³⁴Z. M. Hu, Y. L. Gao, R. S. Myong, H. S. Dou, and B. C. Khoo, "Geometric criterion for RR-MR transition in hypersonic double-wedge flows," *Phys. Fluids* **22**, 016101 (2010).
- ³⁵G. Colonna, M. Tuttafesta, M. Capitelli, and D. Giordano, "Non-Arrhenius NO formation rate in one-dimensional nozzle airflow," *J. Thermophys. Heat Transfer* **13**, 372–375 (1999).
- ³⁶N. Belouaggadia, H. Olivier, and R. Brun, "Numerical and theoretical study of the shock stand-off distance in non-equilibrium flows," *J. Fluid Mech.* **607**, 167–197 (2008).